Tellus SERIES B CHEMICAL AND PHYSICAL METEOROLOGY
PUBLISHED BY THE INTERNATIONAL METEOROLOGICAL INSTITUTE IN STOCKHOLM

Tellus (2009), 61B, 732–746
Printed in Singapore. All rights reserved

© 2009 The Authors
Journal compilation © 2009 Blackwell Munksgaard

TELLUS

Estimating the Asian radon flux density and its latitudinal gradient in winter using ground-based radon observations at Sado Island

By ALASTAIR G. WILLIAMS[1]*, SCOTT CHAMBERS[1], WLODEK ZAHOROWSKI[1], JAGODA CRAWFORD[1], KIYOSHI MATSUMOTO[2] and MITSUO UEMATSU[3], [1]*Australian Nuclear Science and Technology Organisation, PMB 1, Menai, NSW, 2234, Australia;* [2]*Division of Interdisciplinary Sciences, University of Yamanashi, 4-4-37, Takeda, Kofu, 400-8510, Japan;* [3]*Ocean Research Institute, The University of Tokyo, 1-15-1, Minamidai, Nakano-ku, Tokyo, 164-8639, Japan*

(Manuscript received 8 April 2009; in final form 21 July 2009)

ABSTRACT

Terrestrial radon-222 flux density for the Asian continent, integrated over distances of 4500 km, is estimated in two 20° latitudinal bands centred on 48.8°N and 63.2°N. The evaluation is based on three years of wintertime radon measurements at Sado Island, Japan, together with meteorological and trajectory information. A selection of 18% of observations are suitable for evaluation of an analytical expression for the continental surface flux. Various meteorological assumptions are discussed; it is found that there is a substantial effect of increased complexity of the formulation on the flux estimates obtained. The distribution of spatially integrated radon flux over the Asian landmass is reported for the first time. Expressed as geometric means and 1σ-ranges, estimated fluxes are 14.1 mBq m^{-2} s^{-1} (1σ-range: 18 mBq m^{-2} s^{-1}) and 8.4 mBq m^{-2} s^{-1} (1σ-range: 10 mBq m^{-2} s^{-1}) for the lower and higher latitude bands. These results constitute an annual minimum in flux densities for these regions, and are higher than previously reported. The existence of a latitudinal gradient in the continental radon source function is confirmed; the present estimate for Asia (−0.39 mBq m^{-2} s^{-1} per degree of latitude) is in agreement with the northern hemisphere terrestrial radon flux gradient proposed previously.

1. Introduction

Two major factors presently limiting the performance of regional and global weather/climate models on diurnal to seasonal time scales are: (1) the representation of transport and mixing processes in the lower atmosphere; and (2) detailed knowledge of the emissions of climatically significant aerosols and greenhouse gases, both natural and anthropogenic.

The naturally occurring noble gas radon (^{222}Rn) is an effective tracer for both terrestrial air mass movements (Israël, 1951; Polian et al., 1986; Kritz, 1990; Balkanski et al., 1992; Perry et al., 1999) and atmospheric mixing (Wigand and Wenk, 1928; Jacobi and André, 1963; Guedalia et al., 1974; Liu et al., 1984; Butterweck et al., 1994; Lee and Larson, 1997), and its unique physical characteristics have made it a popular tool for the evaluation of transport and mixing schemes in weather, climate and chemical transport models (Jacob et al., 1997; Dentener et al., 1999; Rasch et al., 2000; Chevillard et al., 2002; Gupta et al., 2004; Considine et al., 2005; Forster et al., 2007). Furthermore, since the terrestrial radon source function is relatively simple and similar processes control the surface-atmosphere exchange of radon and certain important greenhouse gases (including CH_4, CO_2 and N_2O), time-series observations of atmospheric radon concentrations together with a companion species of interest can be used to infer regionally integrated emissions of the companion species on seasonal timescales using the radon-calibrated flux technique (Gaudry et al., 1990; Schmidt et al., 1996; Biraud et al., 2000).

Radon is a radioactive gas with a half-life of 3.82 d, comparable to the residence time of key atmospheric pollutants and the synoptic timescale. Being inert and poorly soluble in water (Jacob and Prather, 1990; Li and Chang, 1996), radon is not susceptible to wet or dry atmospheric removal processes. Derived from the long-lived radium-226, present in most rock and soil types, radon's surface flux density is typically between 0.72 and 1.2 atoms cm^{-2} s^{-1} (15–25 mBq m^{-2} s^{-1}) over ice-free terrestrial

*Corresponding author.
e-mail: Alastair.Williams@ansto.gov.au
DOI: 10.1111/j.1600-0889.2009.00438.x

surfaces, and varies mainly geographically as surface soil characteristics change. Over open water bodies, radon emissions are 2–3 orders of magnitude smaller than over land (Turekian et al., 1977; Lambert et al., 1982; Schery and Huang, 2004).

In contemporary attempts to use radon for evaluation of numerical transport and mixing schemes, and for constraining regional inventories of climatically significant species, a significant source of uncertainty can be attributed to geographical variations in the terrestrial radon source function (Lee and Feichter, 1995; Rasch et al., 2000). A number of factors, including radium-226 content, soil type, grain size, water content and ice cover are known to contribute to heterogeneity in the terrestrial radon flux density (Wilkening et al., 1972; Turekian et al., 1977; Nazaroff, 1992), necessitating considerable spatial integration of results in order to derive regionally representative and robust estimates (Zhuo et al., 2008). While Jacob et al. (1997) estimated that the commonly adopted radon source function of 1 atoms cm^{-2} s^{-1} (20.98 mBq m^{-2} s^{-1}) is accurate to about 25% globally, a number of investigators have hypothesized that much of the regional variability is manifest as a latitudinal gradient (e.g. Lee and Feichter, 1995; Schery and Wasiolek, 1998; Giannakopoulos et al., 1999; Conen and Robertson, 2002). Variations in the latitude band between 30°N and 60°N are of particular interest, as this band has the highest land/ocean surface ratio on the globe (Conen and Robertson, 2002) and includes the important boreal forest biome.

With the exception of some studies in China (e.g. Jin et al., 1998; Zhuo et al., 2008), few direct estimates of the radon source function exist for continental Asia east of 60°E and north of 30°N. The use of direct techniques (e.g. accumulation chambers) over such an extensive and largely inaccessible region is both impractical and unlikely to yield results representative of a spatially integrated flux density (Wilkening et al., 1972; Turekian et al., 1977; Hutter and Knutson, 1998). In terms of *indirect* measurements, airborne radon profiles have sometimes been used to infer regionally integrated surface flux densities (Malakhov et al., 1966; Kirichenko, 1970; Larson, 1974). However, such estimates are restricted temporally, are costly to conduct, and assume a balance between the local surface flux density, measured concentrations and decay, which, in practice, is infrequently met. At larger spatial and temporal scales, regional radon flux densities have also been inferred from published rates of ^{210}Pb deposition (e.g. Preiss et al., 1996), although the accuracy of such estimates is likewise compromised by difficulties in justifying the assumptions required.

Based on a combination of direct and indirect methods (including airborne profile measurements in Europe, Russia and North America) and ^{210}Pb deposition studies, Conen and Robertson (2002) estimated a latitudinal gradient in the northern hemisphere terrestrial radon source function that decreased from 1 atoms cm^{-2} s^{-1} at 30°N to 0.2 atoms cm^{-2} s^{-1} at 70°N. However, direct measurements throughout China by Zhuo et al. (2008) indicated that radon flux densities in the vicinity of 43°N are almost 30% higher than the value predicted by Conen and Robertson (2002). With such discrepancies in mind, it is the aim of this study to better constrain the radon source function across continental Asia.

In this paper, we exploit a 3-yr dataset of continuous, hourly radon concentration measurements at a surface site off the East Asian coastline (Sado Island, Japan). Back-trajectory information is used to select subsets of the data representing air masses arriving at Sado during the winter monsoon period that have traversed Asia in an approximately west to east orientation in two latitude bands between 30°N and 70°N. We use supplementary meteorological data to identify important transport and mixing features of the system and to develop assumptions leading to an analytical expression for estimation of the spatially integrated radon flux density in the two latitude bands, and subsequently the latitudinal flux density gradient. We then assess the relative importance of our assumptions and put our flux density estimates in the context of relevant results published by others.

2. Selection and characteristics of winter continental outflow events

2.1. Radon dataset and meteorological input

Hourly atmospheric radon concentrations for 3 yr (2002–2004) were measured at an Acid Deposition and Oxidant Research Centre site on the northwest coast of Sado Island, Japan (38.25°N, 138.4°E). Sado was one of four sites in an Asian-Pacific network of Australian Nuclear Science and Technology Organisation radon detectors that operated continuously during this period. A 750-L dual flow loop two-filter detector was used, with a lower limit of detection of 145 mBq m^{-3}. The average data recovery rate over this period was 93%. The wider context of these radon measurements can be found in Zahorowski et al. (2005) and experimental details are provided in Chambers et al. (2008).

Since collocated meteorological data were not available at Sado, hourly meteorological data and daily radiosonde ascents from the coastal townships of Aikawa (25 km south; 38°01'N, 138°23'E) and Wajima (150 km southwest; 37°23'N, 136°53'E) have been used to supplement the radon measurements (see inset Fig. 1). Daily 09:00 (local standard time) radiosonde soundings from Wajima were analyzed individually for mixing depth/cloud base, cloud top and trade-wind inversion height. Little diurnal variation is experienced in the height of the mixed layer at Wajima in winter when the fetch is oceanic. This is confirmed by inspection of diurnal composite plots of Sado winter radon concentration, the amplitude of which (0.25 Bq m^{-3}) are an order of magnitude smaller than that observed at an inland site near Tokyo (2.56 Bq m^{-3}; Hattori and Ichiji, 1998).

Air-flow patterns were derived from 10-d back trajectories. These were calculated using version 4.6 of NOAA Air Resources Laboratory's (ARL) HYbrid Single-Particle Lagrangian

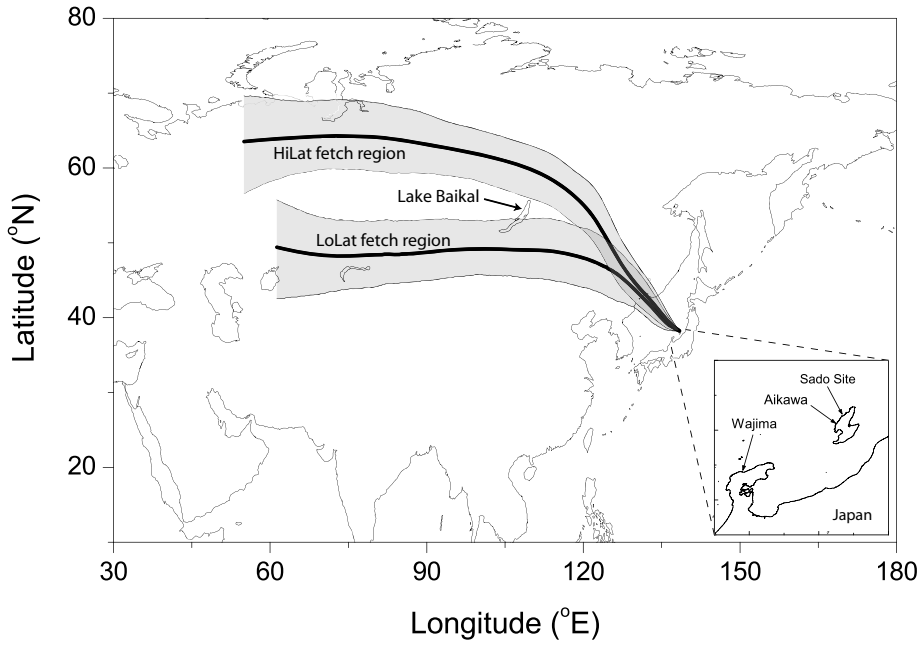

Fig. 1. Asian study region including the lower latitude and higher latitude clusters. Bold lines represent mean trajectories and shaded regions $\pm 1\sigma$ latitude variations. Inset shows sites of radon measurement, hourly meteorological data and radiosonde ascents.

Integrated Trajectory (HYSPLIT) model (Draxler and Hess, 1998). HYSPLIT 4.6 has a total of 20 vertical layers spanning the range 10–11500 m above mean sea level. The meteorological data used by HYSPLIT for its back trajectory calculations are the ARL FNL ('final') data archives, which consist of output from the National Weather Service National Centre for Environmental Prediction's (NCEP) Medium Range Forecast model converted from a $1^\circ \times 1^\circ$ grid to hemispheric 129×129 polar stereographic grids.

2.2. *Continental outflow events*

A climatology and fetch analysis for Sado, presented in Chambers et al. (2008) for the same 3 yr dataset, identified September through April as the period of most consistent continental outflow from Asia, driven by the winter monsoonal circulation. Within this period, mean monthly radon concentrations were highest from November to February, indicating longer land fetches and/or more consistent interaction between air masses and the terrestrial radon source during their passage across Asia. Hence, in the current study, we focus on these 4 months of each year.

Back trajectories were used to select hourly events corresponding to air parcels, which, after traversing the continent, went directly to Sado across the Sea of Japan. The majority of hourly events in the periods under consideration did not fulfil this condition. Furthermore, from this reduced dataset two additional types of event were excluded: (1) where the air after crossing the East Asian coastline did not continue directly to Sado across the Sea of Japan (e.g. made an intermediate landfall); and (2) where, apart from crossing the Sea of Japan, the air mass did not spend its entire 10-d hind-cast period over continental Asia (e.g. remained for a period over the Yellow Sea or passed north of 75°N). The remaining set of 1845 hourly measurements (out of a total 8640) corresponded to trajectories with a broad and relatively even coverage of continental Asia between the latitudes 35°N and 75°N, many of which penetrated the continent to longitudes of between 30°E and 50°E.

Associated meteorological quantities extracted from HYSPLIT, along with the trajectories themselves, included the transit time across the Sea of Japan, and vertical profiles of wind speed and direction at three points of interest: Sado; the trajectory crossing point on the East Asian coast; and the parcel's location 24 h prior to the coastal crossing. The average daytime mixing depth over land was also calculated for each event by identifying daytime segments in each trajectory using an algorithm based on geographical position and local time.

2.3. *Characteristics of the chosen events*

The set of hourly events defined previously was chosen according to broad seasonal and geographic criteria to represent the simplest scenario for evaluation of the continental radon flux density. Nevertheless, these air masses are still influenced by a range of meteorological conditions on their way to the station. In this section we identify the most important of these conditions, which are then accounted for in our estimation of radon flux densities.

The selected trajectories are predominantly oriented west–east between their endpoints and longitudes of 110°E to 120°E, after which they usually turn southeast across northern China before entering the Sea of Japan near Vladivostok. A flow pattern of this kind is generated by the northern arc of the continental anticyclone, often present over Eurasia in the wintertime (Kajii et al., 1997; Merrill et al., 1997). The trajectories were subdivided into two clusters for investigation of the latitudinal dependence of the continental radon flux density. The lower latitude cluster comprised a total of 719 trajectories that spent at least 70% of their time within the latitude band 35°N to 54°N (centred on 48.8°N). The higher latitude cluster comprised a total of 1126 trajectories that spent at least 70% of their time within the latitude band 54°N to 75°N (centred on 63.2°N). Figure 1 shows pertinent features of the continental Asian and Sado regions, as well as average back trajectories in the two clusters.

As can be seen in Fig. 1, the selected air masses spend most of their time over the continent (9 d of the 10-d trajectory, on average). This is sufficient time for radon in the atmospheric column to equilibrate with the (downwind-weighted) average surface source (Malakhov et al., 1966). Under the influence of the Asian winter anticyclone, much of the region experiences large-scale subsidence. In addition, as most of the continent north of 35°N is snow covered during the winter months, the continental boundary layer is likely to have a persistent stable or neutral stratification. Evidence of predominantly stably stratified conditions in the land boundary layer can be seen by the low depth of the mixed layer over land (mean around 450 m) and its narrow distribution, shown in black in Fig. 2. Under these conditions, most of the radon emitted from the Asian surface is expected to remain within the mixed layer, except when it is perturbed by occasional passing frontal systems with associated moist convection.

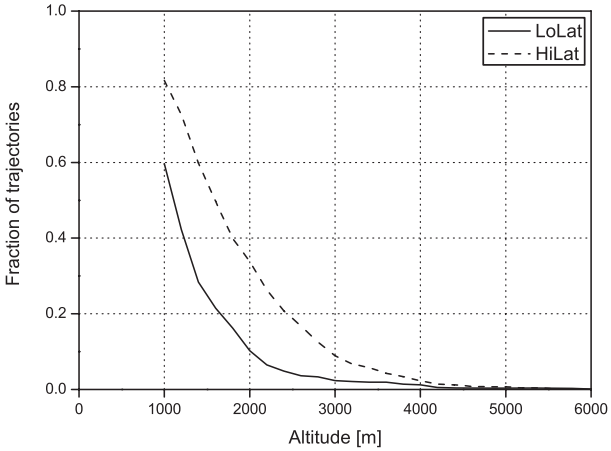

Fig. 3. Fraction of HYSPLIT trajectories in the lower and higher latitude clusters that spend at least 50% of their time above a given altitude.

Many of the HYSPLIT trajectories arriving at Sado have spent a significant fraction of their over-land time in a layer directly above the daytime mixed layer but below 4000 m (Fig. 3). As only a few percent of trajectories penetrate above 4000 m, we take this level as a natural top for our study domain over land. The air in the 'upper' layer is expected to have very different (much lower) radon concentrations to that of the mixed layer below, and it is therefore important that the impact of radon dilution by mixing between the two layers prior to arrival at Sado be considered in our flux analysis. An important parameter distinguishing the two layers, apart from their depths, is the layer-averaged wind speed. This is illustrated in Fig. 4, which

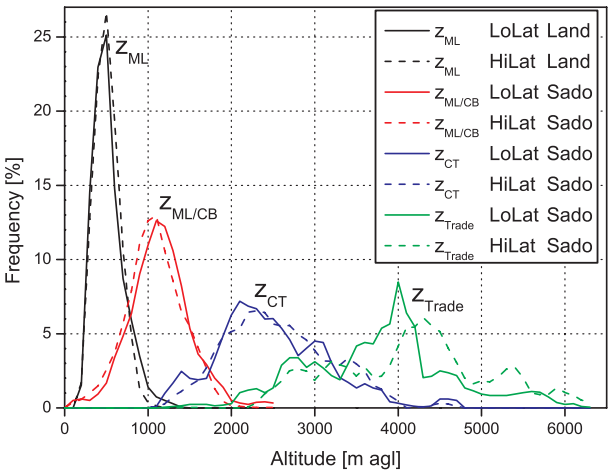

Fig. 2. Histograms of selected heights (z) from HYSPLIT trajectories (Land) and sonde profiles (Sado), for low and high latitude (LoLat / HiLat) trajectory clusters. ML = mixed layer; CB = cloud base; CT = cloud top; Trade = trade wind inversion.

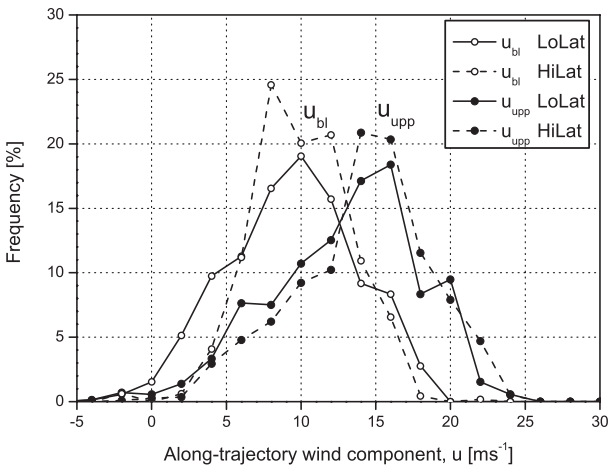

Fig. 4. Histograms of layer-averaged along-trajectory wind components (u_{bl} mixed layer; u_{upp} 'upper' layer) at the point of coastal crossing, from HYSPLIT-derived data along trajectories in the lower and higher latitude clusters.

shows histograms of the vertically integrated HYSPLIT along-trajectory (u-) wind component at the coast. It can be seen that the average u-wind component over land is: (1) significantly (about 5 ms^{-1}) larger in the 'upper' layer than in the mixed layer; and (2) not significantly different between the lower and higher latitude bands.

Although the time taken by air masses to traverse the Sea of Japan is typically less than 24 h, the trajectory air column is subjected to very different meteorological conditions during this period than in the preceding 9 d over land. It is important to represent these conditions properly, as they directly affect radon concentrations measured close to the sea surface at Sado. There are four major effects to consider:

(1) As trajectories cross the East Asian coastline *en route* to Sado, radon from both the land boundary layer and the 'upper' layer is incorporated into the convective marine boundary layer (MBL) that forms over the comparatively warm Sea of Japan. The change in depth of the boundary layer is significant, as can be seen by comparing relevant height histograms in Fig. 2. There is a clear separation between the histogram peaks for the daytime mixed layer height over land (z_{ML}), typically 450 m, and the mixed layer/cloud base height over Sado ($z_{ML/CB}$), around 1000 m.

(2) As the MBL over the Sea of Japan during continental cold air outflow events is strongly convective and humid, it is frequently topped with a significant coupled cloud layer. According to a cloud survey covering the years 1952–1981 by Warren et al. (1988) over the Sea of Japan near Sado in winter, the frequency of cumuloform cloud occurrence is 40% with average cloud coverage of 26%, while the frequency of stratoform clouds is 56% with coverage of 48%. Cloud top heights (z_{CT}) can often reach 2500 m or higher (Fig. 2). As there can be significant vertical transport of radon in coupled cloud layers (Williams et al., 2008), it is important to consider the effects of the entire layer up to cloud top when clouds are present.

(3) Although the cloud top height over Sado is highly variable, it rarely extends beyond 4000 m (Fig. 2). This coincides with the peak in the distribution of the upper (trade wind) inversion height above Sado (z_{Trade} in Fig. 2) and also our chosen domain top over land.

(4) There are no significant differences between the histograms of the two latitudinal trajectory clusters for any of the heights in Fig. 2, indicating that the latitudinal differences in air-mass source do not influence the boundary layer height characteristics at Sado.

3. Estimation of continental surface radon flux density

3.1. General description

Our identification in the previous section of the most significant meteorological effects influencing air parcels travelling to Sado along the chosen trajectories leads naturally to the conceptualization of a box model illustrated schematically in Fig. 5. The entire vertical column up to the model top (h_{top}) is assumed to follow the same trajectory with negligible sideways divergence or mixing. This assumption seems reasonable provided that our choice for h_{top} limits the vertical extent of the box model to the lower troposphere, and is tested further using trajectory wind information (see next section). Two horizontal path segments are considered following each trajectory: the first longer one being over land with a constant surface radon flux density F_{sfce}, followed by a second shorter segment (usually around 24 h) over sea with a surface radon flux density F_{sea}, ending at the Sado measurement site.

Over land, the column up to h_{top} is split vertically into two boxes representing (1) the main daytime/residual boundary layer, with a top at height h_{bl}, and (2) the upper layer directly above with height $h_{upp} = h_{top} - h_{bl}$. Any terrestrial diurnal radon cycle (build-up of radon in a shallow nocturnal boundary layer,

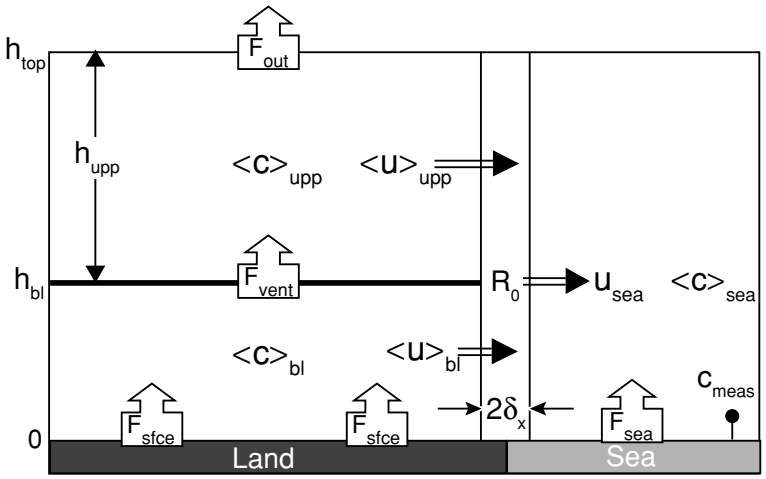

Fig. 5. Schematic of generalized box-model (see text for details).

followed by a morning dilution as the radon mixes up to the top of the new daytime mixed layer) is assumed to be irrelevant to the current problem, as we consider the integrated effect over 10-d trajectories. Radon concentrations over land are assumed to be defined by the balance of flux densities into and out of each box, and the radioactive decay of radon within the box. As we are considering wintertime events only, the amount of radon vented from the top of the land boundary layer ($F_{\rm vent}$) is expected to be small (but not negligible), and only a fraction of this is permanently removed from the top of the model ($F_{\rm out}$). Therefore, the majority of the radon released from the surface over land is ultimately 'channelled' to the air above Sado.

Once the air column reaches the coast, it encounters a relatively warm sea surface. We assume that the two layers that existed over land are mixed into a marine boundary layer that may be topped by active cumulus or stratocumulus clouds and exhibits no diurnal variability. It is further assumed that, while over sea, no radon is lost out of the top of the column and that the flux density out of the sea surface is negligible. Hence, the only assumed change of the total radon within the column as it travels over the sea to the measurement site is due to radioactive decay.

3.2. Budget equations

The vertically-integrated radon budget equation for a column $[z_1, z_2]$ of constant depth $h = z_2 - z_1$, aligned with a trajectory and assuming no vertical mean motion, can be written:

$$\frac{\partial R}{\partial t} = F - \lambda R - \int_{z_1}^{z_2} u \frac{\partial c}{\partial x} dz \tag{1}$$

where $R = \int_{z_1}^{z_2} c(z)dz \equiv h\langle c\rangle$ is the total radon (per unit area) in the column, $c(z)$ is the radon concentration at height z, $\lambda = 2.0982 \times 10^{-6}$ s^{-1} is the radioactive decay constant of radon, u is the along-trajectory horizontal wind component, and $F = F(z_1) - F(z_2)$ is the balance of radon flux densities into the column. Away from the coastal transition, the radon concentration at any given height in the column is expected to change very slowly along the trajectory (over land the column is near-equilibrium, and over sea only decay acts upon the concentration), and we therefore assume the horizontal advection term (3rd term on right-hand side) to be negligible. Equation (1) then has the analytical solution:

$$R = \frac{F}{\lambda} + \left(R_0 - \frac{F}{\lambda}\right) e^{-\lambda(t-t_0)} \tag{2}$$

where $R_0 = R(t_0)$. Assuming equilibrium over land and $F_{\rm sea} = 0$ we can write equations for the total radon in the three model layers of interest (see Fig. 5):

$$R_{\rm bl} \equiv h_{\rm bl}\langle c\rangle_{\rm bl} = \frac{F_{\rm sfce} - F_{\rm vent}}{\lambda} \tag{3}$$

$$R_{\rm upp} \equiv h_{\rm upp}\langle c\rangle_{\rm upp} = \frac{F_{\rm vent} - F_{\rm out}}{\lambda} \tag{4}$$

$$R_{\rm sea} \equiv h_{\rm top}\langle c\rangle_{\rm sea} = R_0 e^{-\lambda t_{\rm sea}} \tag{5}$$

where $t_0 = 0$ is set to be the time at which the trajectory crosses the coast, and $t_{\rm sea}$ is the travel time over the sea surface to the measurement point. R_0 is found by integrating (1), including the advection term, horizontally over a small interval $[-\delta_{\rm x}, \delta_{\rm x}]$ centred on the coast assuming linear variations in c and u, and then taking the limit $\delta_x \to 0$. With the additional continuity constraint along a trajectory, $\frac{\partial}{\partial x}\int_0^{h_{\rm top}} u dz = 0$, we obtain:

$$R_0 = \alpha_{\rm bl} R_{\rm bl} + \alpha_{\rm upp} R_{\rm upp} \tag{6}$$

where

$$\alpha_{\rm bl} = \frac{1}{2}\left(1 + \frac{\langle u\rangle_{\rm bl}}{u_{\rm sea}}\right) \quad \text{and} \quad \alpha_{\rm upp} = \frac{1}{2}\left(1 + \frac{\langle u\rangle_{\rm upp}}{u_{\rm sea}}\right)$$
$$\text{with} \quad u_{\rm sea} = \frac{\langle u\rangle_{\rm bl} h_{\rm bl} + \langle u\rangle_{\rm upp} h_{\rm upp}}{h_{\rm top}} \tag{7}$$

We note that if $\langle u\rangle_{\rm bl} = \langle u\rangle_{\rm upp}$, then $\alpha_{\rm bl} = \alpha_{\rm upp} = 1$ and $R_0 = R_{\rm bl} + R_{\rm upp}$. If we express the flux densities across the top of the boundary layer and the upper layer as fractions of the surface flux density:

$$F_{\rm vent} = \gamma_{\rm v} F_{\rm sfce} \quad \text{and} \quad F_{\rm out} = \gamma_0 F_{\rm vent} = \gamma_0\gamma_{\rm v} F_{\rm sfce} \tag{8}$$

then:

$$F_{\rm sfce} = \frac{\lambda\langle c\rangle_{\rm sea} h_{\rm top} e^{\lambda t_{\rm sea}}}{\alpha_{\rm bl}(1-\gamma_{\rm v}) + \alpha_{\rm upp}\gamma_{\rm v}(1-\gamma_0)} \tag{9}$$

In the above, the venting parameter $\gamma_{\rm v}$ corresponds to the trajectory-integrated fraction of the surface flux density removed from the land boundary layer into the upper layer, and γ_0 corresponds to the fraction of $F_{\rm vent}$ lost from the upper layer out of the model top. As discussed previously, in wintertime anti-cyclonic conditions the boundary layer is expected to be stably stratified much of the time ($F_{\rm vent}$ negligible), interspersed with brief periods of activity corresponding to the passage of fronts and moist convection associated with extra-tropical cyclones ($F_{\rm vent}$ large). The net effect of these processes is expressed via $\gamma_{\rm v}$ and modelled as:

$$\gamma_{\rm v} \equiv \frac{F_{\rm vent}}{F_{\rm sfce}} \approx \frac{f_{\rm cyc} w_{\rm cyc}\left(\langle c\rangle_{\rm bl} - \langle c\rangle_{\rm upp}\right)}{F_{\rm sfce}}$$
$$= \frac{f_{\rm cyc} w_{\rm cyc}}{h_{\rm bl}}\left(\lambda + f_{\rm cyc} w_{\rm cyc}\left(\frac{1}{h_{\rm bl}} + \frac{1-\gamma_0}{h_{\rm upp}}\right)\right)^{-1} \tag{10}$$

where $f_{\rm cyc}$ is the fraction of time spent within the venting portion of an extra-tropical cyclone. We equate $f_{\rm cyc}$ with the fraction of the over-land trajectory segment spent above $z = h_{\rm top}$. The mass flux out of the boundary layer due to an extra-tropical cyclone, expressed as a velocity ($w_{\rm cyc}$), can be approximated using the

results of Cotton et al. (1995):

$$w_{\rm cyc} = \frac{\text{mass flux}}{\text{area} \times \text{air density}} \approx \frac{2.33 \times 10^{10}\,\text{kg s}^{-1}}{1.40 \times 10^{12}\,\text{m}^2 \times 1.225\,\text{kg m}^{-3}} = 0.014\,\text{m s}^{-1} \quad (11)$$

The majority of vertical transport in extra-tropical cyclone systems can be regarded as outflow from a collection of individual deep convection cells of varying heights and maturity. In such situations, a large number of shallow clouds coexist with the deep cumulonimbus clouds but detrain into the lower troposphere above cloud base (our upper layer). This process has been simulated in cumulus ensemble models, for example Yanai et al. (1973) who tuned their simulation to match observed large-scale heat and moisture budgets over an area containing a tropical oceanic cloud cluster. Their derived vertical profiles for cloud detrainment and entrainment (see their Fig. 14) indicated that about 50% of the air entering the cloud system at cloud base ($h_{\rm bl}$) was detrained into the environment above up to about 650 hPa (4000 m). The rest of the air was transported with little further loss up to the tropopause where it was detrained in its entirety. This idealized picture of the detrainment pattern of deep convection systems is consistent with our Fig. 3, which shows that the fraction of trajectories spending significant time above a given height reduces smoothly with height up to 3000–4000 m, but then stays relatively constant above. We thus approximate $\gamma_0 = 0.5$ in our model. As the uncertainty associated with this value is difficult to characterise, we will consider the impact of a large range of γ_0 values from 0.3 to 0.7 in the discussion of our results.

Expressing $\langle c \rangle_{\rm sea}$ by the radon concentrations measured at the surface in Sado ($c_{\rm meas}$) requires integration over radon vertical profiles in the marine boundary layer. Recent high-resolution aircraft measurements of vertical radon profiles in the daytime convective boundary layer (CBL) over land (Williams et al., 2008) have revealed radically different radon concentration profiles in clear and cloudy conditions. In clear sky convective conditions, radon profile shapes vary depending on the strength of mixing (entrainment) across the top of the CBL. Weak entrainment produces profiles that are nearly constant with height, whilst strong entrainment leads to profiles that exhibit significantly reduced radon concentrations in the upper mixed layer. Above the CBL top, radon concentrations drop quickly to low 'background' values that can be as much as two orders of magnitude smaller than in the middle of the mixed layer. In contrast, when the CBL is topped by active cumulus, the cloud-enhanced venting process leads to significant radon concentrations observed in the cloud layer. Under these conditions, radon profiles typically decrease linearly from the surface up to cloud top.

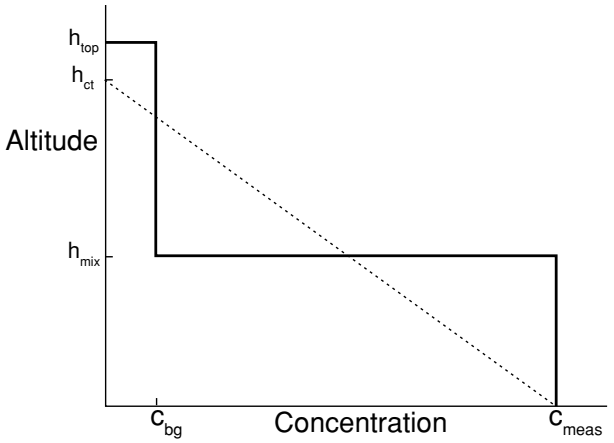

Fig. 6. Assumed vertical profiles for radon in the maritime boundary layer under clear sky (full lines) and cloudy (dotted lines) conditions. $h_{\rm mix}$ = mixed layer top; $h_{\rm ct}$ = cloud top; $h_{\rm top}$ = model top; $c_{\rm bg}$ = background concentration; $c_{\rm meas}$ = measured concentration.

In the present study, the maritime boundary layer under clear skies is likely to have reached an equilibrium depth by the time it reaches Sado, so that entrainment is expected to be small. We therefore postulate a uniformly mixed layer adjacent to the surface, with a decoupled layer immediately above. Our assumed radon profile under clear sky conditions over Sado is thus constant (and equal to the surface value) throughout the mixed layer, with a small background value ($c_{\rm bg}$) above, parameterized as a decayed land upper layer value:

$$c_{\rm bg} \approx \langle c \rangle_{\rm upp}\, e^{-\lambda t_{\rm sea}} \quad (12)$$

As discussed previously, in cloudy conditions we expect a strong coupling between the sub-cloud and cloud layers in the MBL. Hence, we specify a linear decrease for radon from the surface up to cloud top. The assumed vertical profiles for radon in the maritime boundary layer over the Sea of Japan are shown diagrammatically in Fig. 6.

The assumptions discussed above result in the following expression for $\langle c \rangle_{\rm sea}$:

$$\langle c \rangle_{\rm sea} = \begin{cases} c_{\rm meas}\frac{h_{\rm mix}}{h_{\rm top}} + c_{\rm bg}\frac{h_{\rm top}-h_{\rm mix}}{h_{\rm top}} & \text{(clear)} \\ \frac{1}{2}c_{\rm meas}\frac{h_{\rm ct}}{h_{\rm top}} & \text{(cloudy)} \end{cases} \quad (13)$$

where $h_{\rm mix}$ is the mixed layer top in clear conditions and $h_{\rm ct}$ is the cloud top height in cloudy conditions over Sado. Final equations for $F_{\rm sfce}$ are then written as follows:

$$F_{\rm sfce} = \frac{\lambda c_{\rm meas} h e^{\lambda t_{\rm sea}}}{\alpha_{\rm bl}(1-\gamma_{\rm v}) + \alpha_{\rm upp}\gamma_{\rm v}(1-\gamma_0)} f_{\rm adj} \quad (14)$$

$$\text{where}: \begin{cases} h = h_{\rm mix}; & f_{\rm adj} = \left(1 - \frac{h_{\rm top}-h_{\rm mix}}{h_{\rm upp}} \frac{\gamma_{\rm v}(1-\gamma_0)}{\alpha_{\rm bl}(1-\gamma_{\rm v})+\alpha_{\rm upp}\gamma_{\rm v}(1-\gamma_0)}\right)^{-1} & \text{(clear)} \\ h = h_{\rm ct}\ ; & f_{\rm adj} = \frac{1}{2} & \text{(cloudy)} \end{cases}$$

We note that in clear cases a negligible background ($c_{\rm bg} = 0$) is equivalent to setting $f_{\rm adj} = 1$ in the above equation. In the special

case of negligible vertical flux out of the continental boundary layer ($\gamma_v = \gamma_0 = 0$), negligible wind profile effects ($\alpha_{bl} = \alpha_{upp} = 1$) and no radon transport in the cloud layer over Sado, Eq. (14) reduces to:

$$F_0 = \lambda c_{meas} h_{mix} e^{\lambda t_{sea}} \quad (15)$$

For our flux calculations we equated h_{bl} with the HYSPLIT daytime mixed layer heights over land. The Sado mixed layer/cloud base and cloud top heights obtained from the radiosonde data were used for h_{mix} and h_{ct}, respectively. The top of the model we set to a constant $h_{top} = 4000$ m, corresponding to both the average trade wind inversion height and the maximum cloud top height over Sado. As can be seen in Fig. 3, most trajectories spend a significant fraction of their time below 4000 m (98% for the lower and 96% for the higher latitude cluster).

The layer-averaged wind components $\langle u \rangle_{bl}$ and $\langle u \rangle_{upp}$ at the point where the trajectories cross the coast were obtained by vertically integrating coastal wind profiles extracted from HYSPLIT, and then rotating onto the local trajectory direction. In practice, α_{bl} and α_{upp} calculations performed using individual trajectories contain large uncertainties that significantly degrade the quality of the final flux density estimations. For this reason, constant values for α_{bl} and α_{upp} are employed in the model, calculated as average values across the whole dataset:

$$\alpha_{bl} = 0.85; \quad \alpha_{upp} = 1.02 \quad (16)$$

The across-trajectory (v-) wind component, obtained simultaneously with the u-component, was also used to test the 'no sideways divergence' assumption of the flux estimation. In the final model computations, events were excluded for which (at the coast):

$$\langle u \rangle_{bl,upp} < 0 \quad \text{and/or} \quad \left| \langle v \rangle_{bl,upp} \right| > 5 \text{ ms}^{-1} \quad (17)$$

These latter checks reduced the dataset used in the final flux computations by a further 18% (16%) for the lower (higher) latitude cluster, to a total number of 588 (950) events.

4. Results

4.1. Observed Sado surface radon concentrations

Histograms of the measured surface radon concentrations at Sado are shown in Fig. 7 separately for the lower and higher latitude trajectory clusters. As the radon histograms are closer in shape to lognormal than normal distributions, their main characteristics are best summarized using geometric means and 1-σ ranges (width of the geometric 1-σ confidence interval). These are listed in Table 1, along with the corresponding arithmetic means.

The higher latitude cluster clearly exhibits a much sharper peak and a narrower histogram than the lower latitude cluster in both clear and cloudy conditions, and the peak value is shifted towards lower radon values. As there are no significant differences

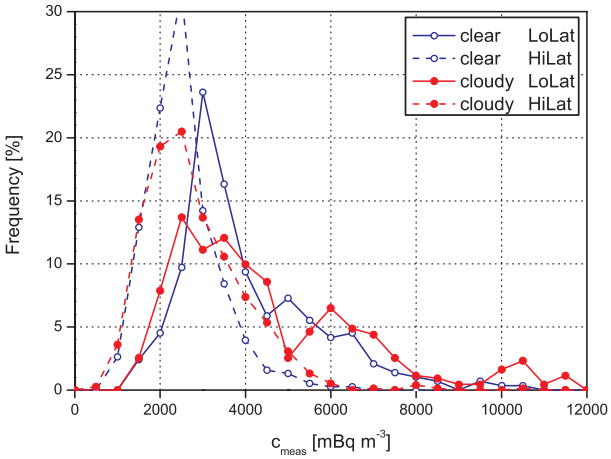

Fig. 7. Measured radon concentration histograms at Sado for lower and higher latitude trajectory clusters, separated into clear sky and cloudy conditions.

observed in the height and wind distribution statistics between the two latitude bands (see Fig. 2 and Fig. 4), it seems likely that the difference observed between the measured radon concentrations from low and high latitudes at Sado is due predominantly to latitudinal variations in the surface source flux density strength and distribution. There are also significant differences in the width of the clear and cloudy histograms in Fig. 7. The greater variability evident in the cloudy histogram is consistent with the idea that, under cloudy conditions, the ground measurements reflect a mixture of air coming from a much larger range of altitudes (up to cloud top). As we do not expect any connection between radon source variations over Asia and meteorological conditions over the Sea of Japan within a given trajectory cluster, it is clear that our confidence in the final flux density estimates will depend strongly on the ability of the box model to resolve these differences.

4.2. Estimated radon flux densities

Figure 8 presents our calculations of the surface radon flux densities over northern Asia using the full box model as described previously. Again, the main characteristics of the resultant histograms are best described using geometric means and 1-σ ranges, and these are listed in Table 1 along with the corresponding arithmetic means. The significantly skewed nature of the observed distributions complicates comparison with the results of others available in the literature, as characteristics of measurement distributions (and the types of mean values quoted) are rarely reported. It should also be noted that, due to the decay of the emitted radon, the computed fluxes represent an average value weighted to the downwind portion of the trajectory.

The model results indicate a clear and significant difference in the radon source distribution between the lower and higher latitude trajectory clusters. Moreover, the model produces

Table 1. Geometric means and widths (1-σ ranges) of radon concentration and computed flux density distributions for two latitude bands over northern Asia. Arithmetic means are also shown, and statistics of some other derived quantities

Quantity	Latitude band	Sado conditions	No. cases (% of all)	Geometric mean	1-σ range	Arithmetic mean
c_{meas}	Lower	Clear	288 (40%)	3479	2940	3785
(mBq m^{-3})		Cloudy	431 (60%)	3751	4011	4275
	Higher	Clear	380 (34%)	2134	1624	2283
		Cloudy	746 (66%)	2288	2171	2531
F_{sfce}	Lower	Clear	240 (41%)	14.2	17.6	16.9
(mBq m^{-2} s^{-1})		Cloudy	348 (59%)	14.1	18.3	17.0
		All	588 (100%)	14.1	18.0	17.0
	Higher	Clear	318 (33%)	7.8	9.1	9.2
		Cloudy	632 (67%)	8.7	10.3	10.2
		All	950 (100%)	8.4	10.0	9.9
F_0	Lower	Clear	288 (40%)	10.7	11.8	12.1
(mBq m^{-2} s^{-1})		Cloudy	431 (60%)	9.3	12.2	11.0
	Higher	Clear	380 (34%)	5.9	5.6	6.5
		Cloudy	746 (66%)	5.5	7.3	6.5

			No. cases (% non-zero)	Arithmetic mean (non-zero only)	Standard deviation
f_{cyc}	Lower	All	719 (15.6%)	0.032 (0.206)	0.113
	Higher	All	1126 (10.9%)	0.028 (0.260)	0.111
γ_v	Lower	All	719 (15.6%)	0.0962 (0.617)	0.2370
	Higher	All	1126 (10.9%)	0.0686 (0.628)	0.2081
$\langle c \rangle_{bl}$	Lower	All	588	15915	10093
(mBq m^{-3})	Higher	All	950	10000	6451
$\langle c \rangle_{upp}$	Lower	All	588 (14.2%)	186 (1299)	598
(mBq m^{-3})	Higher	All	950 (9.4%)	71 (763)	311

almost identical results (in both mean flux densities and histogram widths) from the two independent data subsets representing clear and cloudy conditions over Sado. This outcome inspires confidence in the model's ability to represent the key processes that lead to the significant variations observed in the histograms of Sado radon concentrations (see Fig. 7).

Geometric means and ranges for the calculated radon surface flux densities over the Asian landmass are 14.1 mBq m^{-2} s^{-1} (1σ-range: 18 mBq m^{-2} s^{-1}) and 8.4 mBq m^{-2} s^{-1} (1σ-range: 10 mBq m^{-2} s^{-1}) for the lower and higher latitude bands, respectively. These results are fairly insensitive to reasonable uncertainties in the two main specified parameters, w_{cyc} and γ_0. Sensitivity tests in which w_{cyc} varied from 0.01 to 0.02 and γ_0 varied from 0.3 to 0.7 yielded changes in the computed value of the geometric mean of F_{sfce} that ranged by $\pm$0.50 mBq m^{-2} s^{-1} for the lower and $\pm$0.19 mBq m^{-2} s^{-1} for the higher latitude bands. From the flux densities, we estimate an average radon flux density gradient of around $-$0.39 mBq m^{-2} s^{-1} ($-$0.019 atoms cm^{-2} s^{-1}) per degree of latitude.

The trajectory-derived f_{cyc} values indicate that on average about 3% of trajectory time over land is spent within the venting portion of extra-tropical cyclones (Table 1). However, f_{cyc} is non-zero for only a small fraction of cases (10–15%) for which the average time spent venting is much larger (20–30%). The fraction of air vented out of the boundary layer (γ_v) due to the effects of fronts and deep convection is 7–10% of the surface radon flux density on average, but again this is concentrated into a small

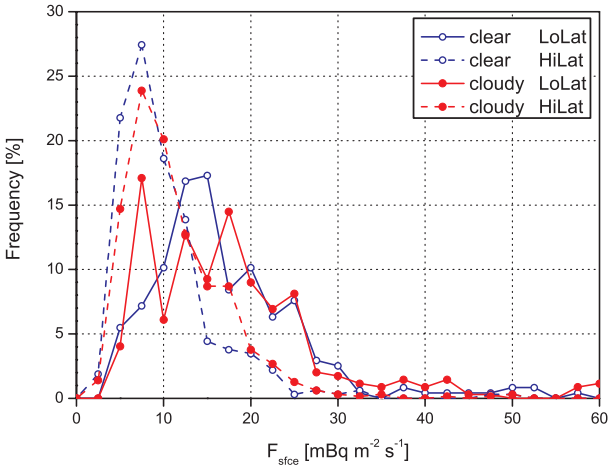

Fig. 8. Histograms of estimated radon flux densities from northern Asia for lower and higher latitude trajectory clusters, separated into clear and cloudy conditions over Sado.

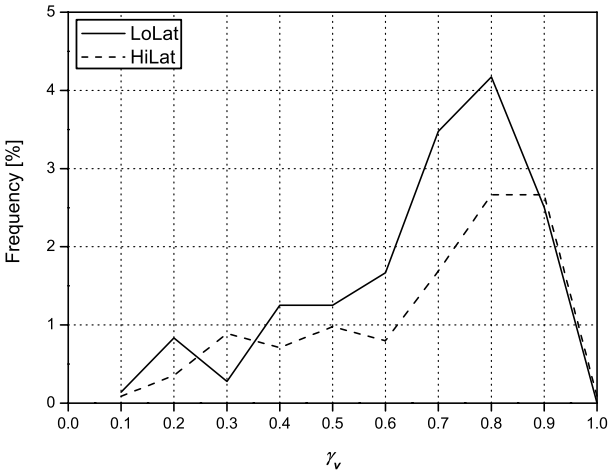

Fig. 9. Histogram of non-zero venting factors for low and high latitude trajectory clusters.

number of non-zero cases for which the γ_v value is much higher. As shown in Fig. 9, the arithmetic mean of non-zero γ_v values is around 62% of F_{sfce}, with the peak at 80%. The small overall venting loss out of the shallow wintertime Asian boundary layer leads to high radon concentrations in the mixed layer ($\langle c \rangle_{bl}$ = 16/10 Bq m^{-3} for the lower/higher latitude band) and relatively small values in the upper layer above ($\langle c \rangle_{upp}$ = 0.2/0.1 Bq m^{-3} on average; 1.3/0.8 Bq m^{-3} during venting episodes). These values are in good agreement with measurements across the Asian continent by Kirichenko (1962), including surface layer radon concentrations in March that varied between 4 and 37 Bq m^{-3} (average 18.1 Bq m^{-3}) and measurements between 3 and 5 km altitude over central Asia in October that yielded a mean radon concentration of 0.27 Bq m^{-3}. The distribution (10th, 50th and 90th percentiles) of radon concentrations observed in winter between 3 and 5 km by Nazarov et al. (1970) in the vicinity of Moscow (at the western extent of our fetch regions) were 0.004, 0.013 and 0.15 Bq m^{-3}, respectively.

5. Discussion

5.1. Impact of model assumptions

The simplest expression to estimate radon flux density, represented by Eq. (15), does not take into account venting of radon over land, wind profile mixing effects, radon distribution in the marine cloud layer or the possibility of non-zero radon background for clear cases over Sado. The resultant F_0 flux density histograms (summarized in Table 1) exhibit significantly lower mean flux densities than those calculated using Eq. (14), which takes into account all the aforementioned effects.

In order to understand the relative importance of various processes and approximations in arriving at the final results discussed above, we have calculated radon flux densities corresponding to five increasingly complex flux estimation methods:

a$_1$:	Simple expression represented by F_0 (Eq. 15).
a$_2$:	As a$_1$, but with the linear radon vertical profile introduced for Sado cloudy cases.
a$_3$:	Venting (γ_v, γ_0) expressions and Sado cloudy radon profiles included, but with negligible radon concentration above the MBL in clear cases ($c_{bg} = 0$) and no wind profile adjustments.
a$_4$:	As a$_3$, but with non-zero c_{bg} in clear cases (c_{bg} and f_{adj} as in Eqs 12 and 14).
final:	Full model, including wind profile adjustments (Eqs 16 and 17). See Fig. 8.

Figure 10 presents the five increasingly complex radon flux estimates calculated for the lower and higher latitude bands. It

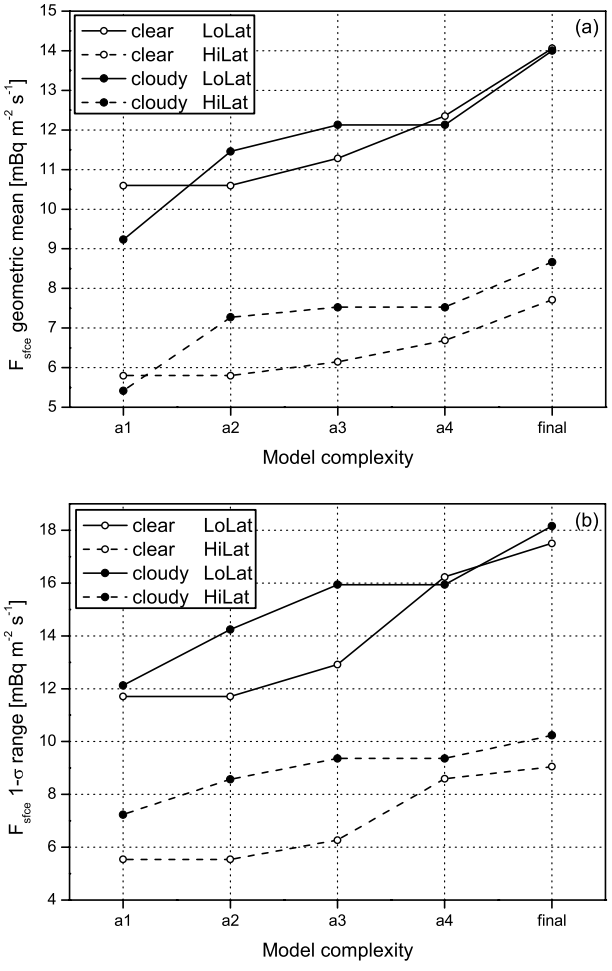

Fig. 10. (a) Geometric means and (b) widths (1σ -ranges), of the surface flux density histograms for a hierarchy of box-model versions, for the lower and higher latitude trajectory clusters, separated into clear and cloudy conditions over Sado.

can be seen that, in each case, inclusion of progressively more realistic representations of physical processes leads to an increase in the mean surface flux densities (Fig. 10a). The distribution of radon up to cloud top (rather than cloud base) in cloudy conditions ($a_1 \rightarrow a_2$), and the addition of a non-zero background radon above the mixed layer top in clear conditions ($a_3 \rightarrow a_4$), both represent an increase in the total amount of radon in the column above Sado ($R_{sea} = h_{top} \langle c \rangle_{sea}$) which then requires a higher flux density over land. On the other hand, the loss of radon by venting processes ($a_2 \rightarrow a_3$), and the disproportionate mixing of faster moving low radon air from the upper layer during the transition to a marine boundary layer over the Sea of Japan ($a_4 \rightarrow$ final), both act to dilute the eventual radon concentrations measured at the surface near Sado. When treatments of the latter processes are introduced into the model, the result is once again an increase in the computed fluxes. The biggest increases in calculated surface flux densities are due to the introduction of the linear radon distribution in cloudy cases ($a_1 \rightarrow a_2$) and the wind profile adjustments ($a_4 \rightarrow$ final).

Each of the improvements introduced into our flux estimates also led to a widening of the computed flux histograms (Fig. 10b). This is a consequence of introducing additional datasets into the model computations, along with their own inherent uncertainties.

The introduction of venting (γ_v, γ_0) in step $a_2 \rightarrow a_3$ resulted in a widening of the flux histograms for all data groupings (Lo/Hi latitude clusters and clear/cloudy conditions). This was caused by uncertainties in γ_v, which are likely to originate from large f_{cyc} variations between trajectories (see Table 1). The addition of wind adjustments in the final step ($a_4 \rightarrow$ final) also led to a widening of all the flux histograms, despite the fact that this step only involved application of constant multiplicative factors (α_{bl} and α_{upp}) in Eq. (14). It may be that these factors acted to amplify the uncertainty in γ_v, or that this effect is a consequence of the reduction in the size of the dataset resulting from the 'no sideways divergence' test in Eq. (17).

The use of estimated cloud top heights in step $a_1 \rightarrow a_2$ led to a widening of the histograms for cloudy cases only. The resultant difference between the widths of the clear and cloudy histograms was removed, however, upon the introduction of a non-zero background radon (c_{bg}) above the mixed layer top for clear cases only in step $a_3 \rightarrow a_4$. Given the definition of c_{bg} (Eq. 12), the additional variability in computed flux densities is likely to have come from changes in $\langle c \rangle_{upp}$ values caused mainly by the fluctuations in γ_v. An important point to note here is that only after consideration of the vertical distribution of radon both within and above the boundary layer was it possible to resolve significant differences in the characteristics of computed Asian radon flux densities for a range of conditions (clear and cloudy) at Sado.

In addition to those discussed previously, there are other more general assumptions made explicitly or implicitly in the model development that may affect our estimates of flux mean and variability. These include:

(1) Loss of memory of radon entering the trajectory column at its western end;

(2) Negligible advection and diffusion of radon laterally into and out of the column as it follows the mean trajectory;

(3) Close relationship between the HYSPLIT model and actual flow trajectories across Asia;

(4) Close relationship between time spent in the venting portion of extra tropical cyclones and fraction of trajectory time spent above model top;

(5) Net effect of other types of meteorological systems extracting radon from the wintertime Asian boundary layer is negligible;

(6) Negligible radon is lost from the model top during the coastal mixing phase and subsequent transit to Sado across the Sea of Japan; and

(7) Idealized radon profiles over the Sado measurement site match well with actual profiles for the specific local conditions selected.

Notwithstanding the above, the results presented in this study offer a first direct experimental estimate of seasonal radon flux density and its geographical variability within the areas concerned.

5.2. *Comparison with other results*

In Fig. 11, results from the current study are compared with others reported in the literature as a function of latitude. It is evident that our estimates lie within the scatter of results summarized by

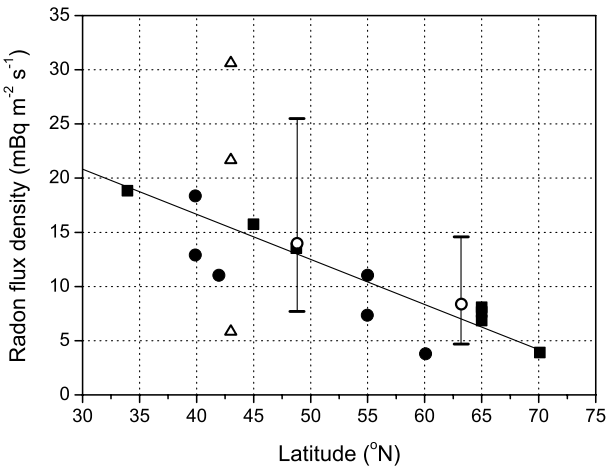

Fig. 11. Radon flux density as a function of latitude. Open circles = current study; solid symbols = Conen and Robertson (2002) review (circles Kirichenko 1970, squares other studies); open triangles = Zhuo et al. (2008); line = radon gradient proposed by Conen and Robertson (2002).

Conen and Robertson (2002) (all solid symbols in Fig. 11), who presented a compilation from five separate studies conducted in different regions of the globe during different times of the year.

In general, there is a qualitative agreement between our results and those summarized by Conen and Robertson (2002). However, it is evident in Fig. 11 that the flux density estimates from the current study, corresponding to wintertime conditions, lie near the upper edge of the envelope of results presented by Conen and Robertson (2002) for all seasons. This apparent discrepancy can be explained by considering the following two factors:

(1) We believe that a subset of the Conen and Robertson (2002) results that were obtained in an area similar to our study domain may have systematically underestimated the surface flux densities. The results, originally published by Kirichenko (1970), inferred radon flux densities by integrating 10–15 point profiles of radon progeny measured in the lower atmosphere using an aircraft. Each of the six solid circles in Fig. 11 represents an average regional radon flux density derived from 5 to 35 individual vertical profiles. Unfortunately, it is not stated whether the averages quoted by Kirichenko represent arithmetic or geometric means. All measurements were conducted within stationary anti-cyclonic northern hemisphere summertime systems avoiding periods of frontal passage, thus ensuring that the predominant removal of radon from the atmospheric column was by radioactive decay only. There are two reasons for which these aircraft results might significantly underestimate the actual flux.

First, the Kirichenko study measured radon progeny rather than radon directly. This can lead to underestimation of the flux in a number of ways: (1) an assumption of equilibrium between radon and its progeny was required; (2) the ultra fine particle fraction ($< 0.1\ \mu$m) was not sampled, as a single progeny filter was used in the aerosol collection; and (3) the presence of clouds was assumed to act only to redistribute the radon progeny within the observed profile, whereas it is well known that clouds can capture a significant fraction of aerosols and (at least temporarily) remove them from circulation within the mixed-layer.

Second, the total column radon activity (and subsequently also the surface flux density) is likely to be underestimated unless each sounding incorporates the complete cloud layer. This has been indicated in recent aircraft measurements of direct radon concentrations (i.e. not progeny) in clear and cloudy convective boundary layers in Australia by Williams et al. (2008).

Given the above, it is not surprising that four of the six flux density estimates by Kirichenko (1970) shown in Fig. 11 lie well below the line presented by Conen and Robertson (2002) as representing the northern hemisphere latitudinal radon flux density gradient.

(2) The apparent discrepancy might also result from a higher mean annual radon flux density in Asia than the northern hemisphere average. This is indeed one of the results of a recent survey conducted by Zhuo et al. (2008). They reported a seasonal amplitude in China's average radon flux density that was 48% of the mean annual value. Summer (high), winter (low) and mean annual values of radon flux density averaged over the Zhuo et al. (2008) regions IV and VI, which border the lower latitude fetch region of this study to the south, are depicted as triangles in Fig. 11. Zhuo et al. note that the fluxes reported in their study are approximately normally distributed. It is immediately seen that the combined envelope of flux density estimates from Conen and Robertson (2002) and the current study falls between the winter and mean annual values presented by Zhuo et al. (2008). While it is unlikely that the radon flux density across central and northern Asia is as heterogeneous as the topographically and geographically complex Chinese region, a seasonal variation in radon flux density from the lower and higher latitude fetch regions should be expected, with a range that is bounded below by the (wintertime) flux density estimates of this study.

We expect that radon flux densities from the lower and higher latitude trajectory clusters—the majority of which are snow-covered and or frozen between November and February of each year—constitute a seasonal minimum in flux density magnitudes for the respective regions. This is because the likely presence of frozen saturated soil effectively prohibits the exhalation of radon from that surface (Turekian et al., 1977; Schery and Huang, 2004). Even the presence of a snow pack alone will lead to some reduction of the radon flux density as demonstrated, for example, by Anderson and Larson (1974), who reported that the presence of a 60 cm snow pack in the Yukon Valley, Alaska, served to reduce the effective radon flux density by 15%.

The smaller spread of flux density values (Fig. 8) in the histograms from the higher latitude band compared with those of the lower latitude band is consistent with expectations that the higher latitudes are characterized by more radon-homogeneous surfaces. The higher latitude band is more topographically homogeneous and includes much of the Asian boreal biome, characterized by high levels of precipitation and poorly drained soils where the mineral horizon is typically covered by substantial amounts of organic material. In contrast, much of the landscape within the lower latitude fetch region is topographically and geologically complex, characterized by a larger proportion of exposed or recently weathered rocks, porous mineral soils and sparser vegetation. The lower latitude band is also in a lower rainfall regime than the higher latitude band.

6. Conclusions

Back trajectories, corresponding to a carefully selected subset of 3 yr of continuous hourly radon observations in the northern hemisphere winter, were clustered into two distinct Asian fetch regions separated by 14.5° of latitude. The predominantly east–west oriented portions of each region extend for a distance of

approximately 4500 km and have a width ($\pm 1\sigma$ in latitude from the cluster mean) of approximately 700 km.

The radon observations corresponding to the two fetch regions constitute approximately 18% of all wintertime events, and were specifically chosen to justify the application of a simple box model for estimations of the continental radon flux density. We have shown that an analytical expression for the flux can be successfully developed and applied, provided that careful attention is paid to the validity of assumptions and estimations regarding: (1) the meteorological conditions encountered by air parcels following trajectories across a region of interest (including venting processes and vertical variations in the wind profile), and (2) the form of the vertical concentration profiles above the final measurement site. The effects of each assumption on the final numerical results were individually quantified in this study, enabling an assessment of the relative importance of including these processes in such computations.

The distribution of the spatially integrated radon flux density over the Asian landmass is reported for the first time in this study. The significantly skewed nature of the observed distributions complicates comparison with the results of others available in the literature, as characteristics of measurement distributions (and the types of mean values quoted) are rarely reported. Geometric means and 1σ-ranges for the estimated fluxes have been found to be equal to 14.1 mBq m^{-2} s^{-1} (1σ-range: 18 mBq m^{-2} s^{-1}) and 8.4 mBq m^{-2} s^{-1} (1σ-range: 10 mBq m^{-2} s^{-1}) for the lower and higher latitude bands, respectively. These results, which constitute an annual minimum in flux densities for the respective regions, are higher than those reported previously (Conen and Robertson, 2002). This appears to indicate that the magnitude of terrestrial radon fluxes across Asia is greater than the northern hemisphere average.

The spatially integrated mean radon flux density estimates clearly confirm the existence of a latitudinal gradient in the terrestrial radon source function as postulated by Lee and Feichter (1995), Schery and Wasiolek (1998), Conen and Robertson (2002) and others. Furthermore, our estimate of the latitudinal gradient across Asia (-0.39 mBq m^{-2} s^{-1} per degree of latitude) is in good agreement with the northern hemisphere terrestrial radon flux density gradient proposed by Conen and Robertson (2002) (-0.42 mBq m^{-2} s^{-1} per degree of latitude).

The spread in the estimated flux density histograms includes a non-negligible component originating from uncertainties in the model assumptions and estimations, and in the supplementary datasets used in the model computations (including the trajectory information). As a result, the σ-values presented should be regarded as representing an outer constraint on the geographical radon flux density variability within the areas of interest.

Finally, we note that it would be instructive to compare the current approach, which applies a simple analytical expression to a small data subset satisfying very stringent applicability criteria, with more complex methods based upon inverse and adjoint modelling (e.g. Vautard et al., 2000; Kurokawa et al., 2009). Although such techniques have the potential to resolve regional source functions for all seasons with a greater spatial resolution than the current method, their success is critically sensitive to the spatiotemporal coverage of observations, the complexity of the species of interest and to uncertainties and biases in the transport models employed (Gurney et al., 2002; Lin et al., 2006; Geels et al., 2007). Nevertheless, some regional studies have been successfully conducted using as few as 4–8 sites (Roustan and Bocquet, 2006; Tanimoto et al., 2008), and given the simplicity of radon compared with other species, it may therefore be possible to constrain its source function using continuous time series observations at only a few observation points. As outlined in Zahorowski et al. (2005) and Chambers et al. (2008), apart from the observations at Sado Island, multi-year datasets of hourly radon concentrations are also available at three other sites strongly influenced by the Asian region (Hok Tsui in Hong Kong; Jeju Island in South Korea; and Mauna Loa in Hawaii). Back trajectory analysis has indicated that there is considerable overlap in the 4–10 d fetch regions for these sites.

References

Anderson, R. V. and Larson, R. E. 1974. Atmospheric electric and radon profiles over a closed basin and the open ocean. *J. Geophys. Res.* **79**(24), 3432–3435.

Balkanski, Y. J., Jacob, D. J., Arimoto, R. and Kritz, M. A. 1992. Distribution of ^{222}Rn over the North Pacific: implications for continental influences. *J. Atmos. Chem.* **14**, 353–374.

Biraud, S., Ciais, P., Ramonet, M. and Simmonds, P. 2000. European greenhouse gas emissions from continuous atmospheric measurements and radon 222 at Mace Head, Ireland. *J. Geophys. Res.* **105**(D1), 1351–1366.

Butterweck, G., Reineking, A., Kesten, J. and Porstendörfer, J. 1994. The use of the natural radioactive noble gases radon and thoron as tracers for the study of turbulent exchange in the atmospheric boundary layer—case study in and above a wheat field. *Atmos. Env.* **28**(12), 1963–1969.

Chambers, S., Zahorowski, W., Matsumoto, K. and Uematsu, M. 2008. Seasonal variability of radon-derived fetch regions for Sado Island, Japan, based on 3 years of observations: 2002–2004. *Atmos. Env.* **43**, 271–279.

Chevillard, A., Ciais, P., Karstens, U., Heimann, M., Schmidt, M. and co-authors. 2002. Transport of ^{222}Rn using the regional model REMO: a detailed comparison with measurements over Europe. *Tellus* **54B**, 850–871.

Conen, F. and Robertson, L. B. 2002. Latitudinal distribution of radon-222 flux from continents. *Tellus* **54B**, 127–133.

Considine, D. B., Bergmann, D. J. and Liu, H. 2005. Sensitivity of global modeling initiative chemistry and transport model simulations of radon-222 and lead-210 to input meteorological data. *Atm. Chem. Phys.* **5**, 3389–3406.

Cotton, W. R., Alexander, G. D., Hertenstein, R., Walko, R. L., McAnelly, R. L. and co-authors. 1995. Cloud venting—a review and some new global annual estimates. *Earth Sci. Rev.* **39**, 169–206.

Dentener, F., Feichter, J. and Jeuken, A. 1999. Simulation of the transport of ^{222}Rn using on-line and off-line global models at different

horizontal resolutions: a detailed comparison with measurements. *Tellus* **51B**, 573–602.

Draxler, R. R. and Hess, G. D. 1998. An overview of the HYSPLIT-4 modelling system for trajectories, dispersion and deposition. *Aust. Met. Mag.* **47**, 295–308.

Forster, C., Stohl, A. and Seibert, P. 2007. Parameterization of convective transport in a lagrangian particle dispersion model and its evaluation. *J. Appl. Met. Clim.* **46**, 403–422.

Gaudry, A., Polian, G., Ardouin, B. and Lambert, G. 1990. Radon-calibrated emissions of CO_2 from South Africa. *Tellus* **42B**, 9–19.

Geels, C., Gloor, M., Ciais, P., Bousquet, P., Peylin, P. and co-authors. 2007. Comparing atmospheric transport models for future regional inversions over Europe—Part 1: mapping the atmospheric CO2 signals. *Atmos. Chem. Phys.* **7**, 3461–3479.

Giannakopoulos, C., Chipperfield, M. P., Law, K. S. and Pyle, J. A. 1999. Validation and intercomparison of wet and dry deposition schemes using ^{210}Pb in a global three-dimensional off-line chemical transport model. *J. Geophys. Res.* **104**(D19), 23761–23784.

Guedalia, D., Allet, C. and Fontan, J. 1974. Vertical exchange measurements in the lower troposphere using ThB (Pb-212) and Radon (Rn-222). *J. Appl. Met.* **13**, 27–39.

Gupta, M. L., Douglass, A. R., Randolph Kawa, S. and Pawson, S. 2004. Use of radon for evaluation of atmospheric transport models: sensitivity to emissions. *Tellus* **56B**, 404–412.

Gurney, K. R., Law, R. M., Denning, A. S., Rayner, P. J., Baker, D. and co-authors. 2002. Towards robust regional estimates of CO2 sources and sinks using atmospheric transport models. *Nature* **415**(6872), 626–630.

Hattori, T. and Ichiji, T. 1998. Estimates of seasonal variations of ^{222}Rn from different origins by using the correlation between ^{222}Rn and ^{212}Pb concentrations in air. In: *Radon and thoron in the human environment* (eds. A. Katase and M. Shimo). World Scientific Publishing Co. Pte. Ltd., Singapore, 246–251.

Hutter, A. R. and Knutson, E. O. 1998. An international intercomparison of soil gas radon and radon exhalation measurements. *Health Phys.* **74**, 108–114.

Israël, H. 1951. Radioactivity of the atmosphere. In: *Compendium of meteorology* (ed. T. F. Malone). American Meteorological Society, Washington, DC, 155–161.

Jacob, D. J. and Prather, M. J. 1990. Radon-222 as a test of convective transport in a general circulation model. *Tellus*, **42B**, 118–134.

Jacob, D. J., Prather, M. J., Rasch, P. J., Shia, R.-L., Balkanski, Y. J. and co-authors. 1997. Evaluation and intercomparison of global atmospheric transport models using ^{222}Rn and other short-lived tracers. *J. Geophys. Res.* **102**(D5), 5953–5970.

Jacobi, W. and André, K. 1963. The vertical distribution of radon 222, radon 220 and their decay products in the atmosphere. *J. Geophys. Res.* **68**(13), 3799–3814.

Jin, Y., Iida, T., Wang, Y. I. Z. and Abe, S. 1998. A subnationwide survey of outdoor and indoor ^{222}Rn concentrations in China by passive method. In: *Radon and thoron in the human environment. Proceedings of the 7th Tohwa University International Symposium* (eds. A. Katase and M. Shimo). World Scientific Publishing Co. Pte. Ltd, Singapore, 276–281.

Kajii, Y., Akimoto, H., Komazaki, Y., Tanaka, S., Mukai, H. and co-authors. 1997. Long-range transport of ozone, carbon monoxide, and acidic trace gases at Oki Island, Japan, during PEM-West B; PEACAMPOT B campaign. *J. Geophys. Res.* **102**(D23), 28637–28649.

Kirichenko, L. V. 1962. The vertical distribution of the products of decay of radon in the free atmosphere. In: *Problems of nuclear meteorology* (eds. I. L. Karol and S. G. Malakhov). United States Atomic Energy Commission, Division of Technical Information, AEC-TR-6128, 92–124.

Kirichenko, L. V. 1970. Radon exhalation from vast areas according to vertical distributions of its short-lived decay products. *J. Geophys. Res.* **75**(18), 3639–3649.

Kritz, M. A. 1990. The China clipper—fast advective transport of radon-rich air from the Asian boundary layer to the upper troposphere near California. *Tellus*, **42B**, 46–61.

Kurokawa, J., Yumimoto, K., Uno, I. and Ohara, T. 2009. Adjoint inverse modeling of NOx emissions over eastern China using satellite observations of NO2 vertical column densities. *Atmos. Environ.* **43**, 1878–1887.

Lambert, G., Polian, G., Sanak, J., Ardouin, B., Buisson, A. and co-authors. 1982. Cycle du radon et de ses descentants: application à l'étude des échanges troposphère-stratosphère. *Ann. Géophys.* **38**(4), 497–531.

Larson, R. E. 1974. Radon profiles over Kilauea, the Hawaiian Islands, and Yukon Valley snow cover. *Pure Appl. Geophys.* **112**, 204–208.

Lee, H. N. and Feichter, J. 1995. An intercomparison of wet precipitation scavenging schemes and emission rates of ^{222}Rn for the simulation of global transport and deposition of ^{210}Pb. *J. Geophys. Res.* **100**(D11), 23253–23270.

Lee, H. N. and Larson, R. J. 1997. Vertical diffusion in the lower atmosphere using aircraft measurements of ^{222}Rn. *J. Appl. Meteorol.* **36**, 1262–1270.

Li, Y. and Chang, J. S. 1996. A three-dimensional global episodic tracer transport model: 1 Evaluation of its transport processes by radon 222 simulations. *J. Geophys. Res.* **101**(D20), 25931–25947.

Lin, J. C., Gerbig, C., Wofsy, S. C., Daube, B. C., Matross, D. M. and co-authors. 2006. What have we learned from intensive atmospheric sampling field programmes of CO2? *Tellus* **58B**, 331–343.

Liu, S. C., McAfee, J. R. and Cicerone, R. J. 1984. Radon 222 and tropospheric vertical transport. *J. Geophys. Res.* **89**(D5), 7291–7297.

Malakhov, S. G., Bakulin, V. N., Dmitrieva, G. V., Kirichenko, L. V., Sisigina, T. I., and co-authors. 1966. Diurnal variations of radon and thoron decay product concentrations in the surface layer of the atmosphere and their washout by precipitation. *Tellus* **18**, 643–654.

Merrill, J. T., Newell, R. E. and Bachmeier, A. S. 1997. A meteorological overview for the Pacific Exploratory Mission-West Phase B. *J. Geophys. Res.* **102**(D23), 28241–28253.

Nazaroff, W. W. 1992. Radon transport from soil to air. *Rev. Geophys.* **30**, 137–160.

Nazarov, L. E., Kuzenkov, A. F., Malakhov, S. G., Volokitina, L. A., Gaziyev, Y. I., and co-authors. 1970. Radioactive aerosol distribution in the middle and upper troposphere over the USSR in 1963–1968. *J. Geophys. Res.* **75**(18), 3575–3588.

Perry, K. D., Cahill, T. A., Schnell, R. C. and Harris, J. M. 1999. Long-range transport of anthropogenic aerosols to the National Oceanic and Atmospheric Administration baseline station at Mauna Loa Observatory, Hawaii. *J. Geophys. Res.* **104**(D15), 18521–18533.

Polian, G., Lambert, G., Ardouin, B. and Jegou, A. 1986. Long-range transport of continental radon in subantarctic and arctic areas. *Tellus* **38B**, 178–189.

Preiss, N., Mélières, M.-A. and Pourchet, M. 1996. A compilation of data on lead 210 concentration in surface air and fluxes at the

air-surface and water-sediment interfaces. *J. Geophys. Res.* **101**(D22), 28847–28862.

Rasch, P. J., Feichter, J., Law, K. S., Mahowald, N. M., Penner, J. E. and co-authors. 2000. A comparison of scavenging and deposition processes in global models: results from the WCRP Cambridge Workshop of 1995. *Tellus* **52B**, 1025–1056.

Roustan, Y. and Bocquet, M. 2006. Inverse modelling for mercury over Europe. *Atmos. Chem. Phys.* **6**, 3085–3098.

Schery, S. D. and Huang, S. 2004. An estimate of the global distribution of radon emissions from the ocean. *Geophys. Res. Lett.* **31**, L19104, 1–4.

Schery, S. D. and Wasiolek, M. A. 1998. Modeling radon flux from the earth's surface. In: *Radon and Thoron in the human environment* (eds. A. Katase and M. Shimo). Proceedings of the 7th Tohwa University International Symposium, Fukuoka, Japan, World Scientific Publishing Co. Pte. Ltd, Singapore, 207–217.

Schmidt, M., Graul, R., Sartorius, H. and Levin, I. 1996. Carbon dioxide and methane in continental Europe: a climatology and ^{222}Rn-based emission estimates. *Tellus* **48B**, 457–473.

Tanimoto, H., Sawa, Y., Yonemura, S., Yumimoto, K., Matsueda, H., and co-authors. 2008. Diagnosing recent CO emissions and ozone evolution in East Asia using coordinated surface observations, adjoint inverse modeling, and MOPITT satellite data. *Atmos. Chem. Phys.* **8**(14), 3867–3880.

Turekian, K. K., Nozaki, Y. and Benninger, L. K. 1977. Geochemistry of atmospheric radon and radon products. *Ann. Rev. Earth Planet. Sci.* **5**, 227–255.

Vautard, R., Beekmann, M. and Menut, L. 2000. Applications of adjoint modelling in atmospheric chemistry: sensitivity and inverse modelling. *Environ. Model. Softw.* **15**, 703–709.

Warren, S. G., Hahn, C. J., London, J., Chervin, R. M. and Jenne, R. L. 1988. Global distribution of total cloud cover and cloud type amounts over the ocean. NCAR Technical Note, DOE/ER-0406, NCAR/TN-317+STR. National Center for Atmospheric Research, Boulder, Colorado.

Wigand, A. and Wenk, F. 1928. Der gehalt der luft an radium-emanation, nach Messungen bei Flugzeugaufstiegen. *Ann. Phys.* **86**(13), 657–686.

Wilkening, M. H., Clements, W. E. and Stanley, D. 1972. Radon-222 flux measurements in widely separated regions. In: *The Natural Radiation Environment II*. Proceedings of the 2nd International Symposium on the Natural Radiation Environment, 7–10 August, Houston, Texas, 717–730.

Williams, A. G., Zahorowski, W., Chambers, S., Hacker, J. M., Schelander, P., Element, A., and co-authors. 2008. Mixing and venting in clear and cloudy boundary layers using airborne radon measurements. Proceedings of the 18th American Meteorological Society Symposium on Boundary Layers and Turbulence, Stockholm, Sweden, 9–13 June 2008. Conference paper 9B.4, 1–5. http://ams.confex.com/ams/pdfpapers/139974.pdf or available from corresponding author.

Yanai, M. S., Esbensen, S. and Chu, J. H. 1973. Determination of bulk properties of tropical cloud clusters from large-scale heat and moisture budgets. *J. Atmos. Sci.* **30**, 611–627.

Zahorowski, W., Chambers, S., Wang, T., Kang, C.-H., Uno, I. and co-authors. 2005. Radon-222 in boundary layer and free tropospheric continental outflow events at three ACE-Asia sites. *Tellus* **57B**, 124–140.

Zhuo, W., Guo, Q., Chen, B. and Cheng, G. 2008. Estimating the amount and distribution of radon flux density from the soil surface in China. *J. Env. Rad.* **99**, 1143–1148.